



Article

Oxygen-Deficient WO₃/TiO₂/CC Nanorod Arrays for Visible-Light Photocatalytic Degradation of Methylene Blue

Liaochuan Jiang ^{1,†}, Xingyuan Gao ^{1,2,†} , Shaoling Chen ¹, Jangam Ashok ³ and Sibudjing Kawi ^{3,*} 

¹ Faculty of Chemistry and Material Science, Guangdong University of Education, Guangzhou 510303, China; jiangliaochuan@gdei.edu.cn (L.J.); gaoxingyuan@gdei.edu.cn (X.G.); chenshaoling@gdei.edu.cn (S.C.)

² Engineering Technology Development Center of Advanced Materials & Energy Saving and Emission Reduction in Guangdong Colleges and Universities, Guangzhou 510303, China

³ Department of Chemical and Biomolecular Engineering, National University of Singapore, Singapore 117585, Singapore; jangam.ashok@nus.edu.sg

* Correspondence: chekawis@nus.edu.sg; Tel.: +65-65166312

† The authors contribute equally to this article.

Abstract: At present, TiO₂ is one of the most widely used photocatalytic materials. However, the narrow response range to light limits the photocatalytic performance. Herein, we reported a successful construction of self-doped R-WO₃/R-TiO₂/CC nanocomposites on flexible carbon cloth (CC) via electrochemical reduction to increase the oxygen vacancies (O_{vs}), resulting in an enhanced separation efficiency of photo-induced charge carriers. The photocurrent of R-WO₃/R-TiO₂/CC at −1.6 V (vs. SCE) was 2.6 times higher than that of WO₃/TiO₂/CC, which suggested that O_{vs} could improve the response to sunlight. Moreover, the photocatalytic activity of R-WO₃/TiO₂/CC was explored using methylene blue (MB). The degradation rate of MB could reach 68%, which was 1.3 times and 3.8 times higher than that of WO₃/TiO₂/CC and TiO₂/CC, respectively. Furthermore, the solution resistance and charge transfer resistance of R-WO₃/R-TiO₂/CC were obviously decreased. Therefore, the electrochemical reduction of nanomaterials enabled a promoted separation of photogenerated electron–hole pairs, leading to high photocatalytic activity.

Keywords: photocatalysis; electrochemical reduction; photocatalytic degradation; TiO₂; WO₃



Citation: Jiang, L.; Gao, X.; Chen, S.; Ashok, J.; Kawi, S. Oxygen-Deficient WO₃/TiO₂/CC Nanorod Arrays for Visible-Light Photocatalytic Degradation of Methylene Blue. *Catalysts* **2021**, *11*, 1349. <https://doi.org/10.3390/catal11111349>

Academic Editors: Zsolt Pap, Lucian Baia, Monica Baia and Detlef W. Bahnemann

Received: 14 August 2021

Accepted: 3 November 2021

Published: 9 November 2021

Publisher's Note: MDPI stays neutral with regard to jurisdictional claims in published maps and institutional affiliations.



Copyright: © 2021 by the authors. Licensee MDPI, Basel, Switzerland. This article is an open access article distributed under the terms and conditions of the Creative Commons Attribution (CC BY) license (<https://creativecommons.org/licenses/by/4.0/>).

1. Introduction

The rapid industrial development and urban construction aggravate water pollution, such as organic pollutants, which adds to the pressures on water treatment [1,2]. Traditional wastewater treatment methods still have their shortcomings. For example, physical methods can only transfer harmful substances instead of completely eliminating the pollutants; on the other hand, the sensitivity and efficiency for treatment of low concentrations of organic pollutants are relatively low. In recent years, increasing attention has been paid to novel water treatment technologies, such as electrochemical oxidation and photocatalytic oxidation [3].

Photocatalytic oxidation mainly refers to the conversion of organic pollutants to non-toxic substances such as carbon dioxide, water, and inorganic substances via an oxidation and decomposition reaction under light and normal temperature/pressure [4]. Titanium dioxide (TiO₂) has become one of the most important photocatalysts, because of its high photocatalytic activity and good chemical stability, along with its low cost, non-toxicity, and strong photocorrosion resistance [5–12]. However, inherent properties of TiO₂, such as the large band gap, small response range to light, and recombination of electron–hole pairs, hinder large-scale application, so it is necessary to explore new photocatalysts to obtain optimal photocatalytic performance [13–16].

A variety of methods have been proposed to improve photocatalytic performance. Ion doping on/in the semiconductor surface, gap, or lattice generates defects and changes

the degree of crystallinity, which retards the recombination of charge carriers [17–20]. In addition, noble metal deposition on the surface of TiO_2 materials can promote the separation of photoinduced electron–hole pairs by changing the electron distribution [21]. Surface photosensitization is another strategy to adsorb dye molecules on the exterior of photocatalytic materials, and visible light could be absorbed by the dyes, thus widening the light absorption range of materials. In comparison, semiconductor composites can make use of the heterojunction formed by different materials, so a semiconductor with a wide band gap can be sensitized by the narrow band gap semiconductor, so as to improve the photocatalytic performance as a result of the synergistic effects [19,20].

Various transition metal oxides have been or can be potentially applied to form a composite with TiO_2 , such as WO_3 , ZnO , and Cu_2O [22–32]. In contrast, WO_3 is widely used in the photocatalytic degradation of organic pollutants due to its good photocorrosion resistance, narrow band gap, and admirable conductivity [33–35]. The combination of narrow-band-gap semiconductor WO_3 and wide-band-gap semiconductor TiO_2 enlarges the light absorption range, inhibits the recombination of photogenerated electrons and holes, accelerates the transport and separation of charges, and enhances the photocatalytic efficiency [36]. In addition, the self-doped effect with a lattice defect formed by oxygen vacancies is beneficial to improve the photocatalytic performance of semiconductors. For metal oxides, the lattice oxygen atoms can be partially removed by an electrochemical reduction to produce oxygen vacancies (O_{vs}), which expedite the charge transfer and separation.

Considering the difficulty of separating and recovering the TiO_2 powder from the solution after the degradation reaction, TiO_2 can be coated on the substrate in order to improve the reusability and reduce the cost of the separation process [37]. Moreover, TiO_2 loaded on large-area-functionalized carbon fibers to form nanocomposites has many advantages. Carbon fibers can act as the pollutant concentration agent and supporting material, and the photogenerated electrons of TiO_2 can rapidly transfer along carbon fibers so as to speed up the purification process and obtain high photocatalytic efficiency [38].

In this paper, a cathodic reduction self-doping method was proposed to introduce O_{vs} into $\text{WO}_3/\text{TiO}_2/\text{CC}$ composite films to obtain $\text{R-WO}_3/\text{R-TiO}_2/\text{CC}$. The doping of the composite materials can be easily completed within a few minutes and the number of O_{vs} could be adjusted by the applied potentials. It was found that the catalytic performance of $\text{R-WO}_3/\text{TiO}_2/\text{CC}$ was substantially higher than that of its counterparts, $\text{WO}_3/\text{TiO}_2/\text{CC}$ and TiO_2/CC .

2. Results and Discussion

2.1. XRD Analysis

Figure 1 shows the X-ray diffraction pattern of $\text{WO}_3/\text{TiO}_2/\text{CC}$ and $\text{R-WO}_3/\text{R-TiO}_2/\text{CC}$ composites. It can be seen that the peaks with 2θ degrees of 27.45° , 36.09° , 41.23° , 44.05° , 54.32° , 56.64° , 62.74° , 64.04° , 69.01° , and 72.41° correspond to (1 1 0), (1 0 1), (1 1 1), (2 1 0), (2 1 1), (2 2 0), (0 0 2), (3 1 0), (3 0 1), and (3 1 1) of the TiO_2 crystal plane (PDF NO. 21–1276). Moreover, the peaks at 23.64° , 24.37° , 28.87° , 29.06° , 41.99° , 44.55° , and 50.89° correspond to (0 2 0), (2 0 0), (1 1 2), (1 -1 2), (-2 -2 2), and (3 2 0), (3 2 2) of the WO_3 (PDF NO. 20–1323) crystal plane. In addition, the XRD of as-prepared nanocomposite contains the characteristic diffraction peaks of both TiO_2 and WO_3 , which indicates that $\text{WO}_3/\text{TiO}_2/\text{CC}$ and $\text{R-WO}_3/\text{TiO}_2/\text{CC}$ composite photocatalytic materials were successfully prepared.

2.2. SEM and Photocurrent Response of $\text{WO}_3/\text{TiO}_2/\text{CC}$

2.2.1. SEM Characterization

Figure 2A shows quadrangular prism-shaped TiO_2 nanorods with a smooth lateral surface and spinal top, which is densely grown on carbon fiber. From Figure 2B–F, one can see that the surface of TiO_2 became rougher, and the thickness of WO_3 gradually increased with the augmentation of the current density, which indicates a successful deposition of WO_3 on TiO_2 . When the cathodic current density is -16 mA/cm^2 , TiO_2 nanorods

are uniformly covered with a layer of WO_3 film, as shown in Figure 2F. The thickness of the deposition layer may affect the photoelectrochemical performance. Thinner WO_3 film can provide fewer photoinduced electrons, while thicker WO_3 film may prevent light transmission and reduce the light utilization of TiO_2 , resulting in a decrease in photocurrent.

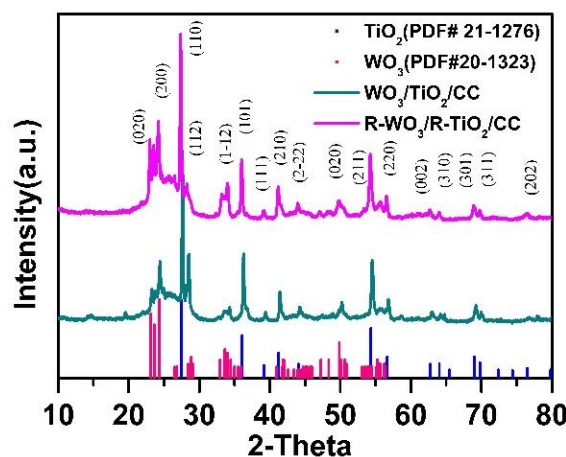


Figure 1. XRD pattern of $\text{WO}_3/\text{TiO}_2/\text{CC}$ and $\text{R-WO}_3/\text{R-TiO}_2/\text{CC}$ composite.

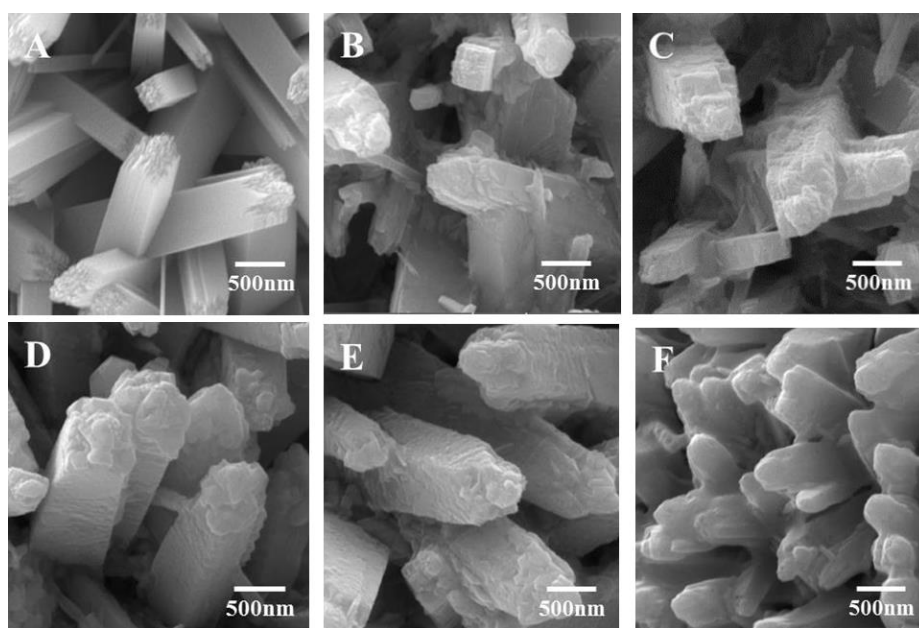


Figure 2. SEM images of $\text{WO}_3/\text{TiO}_2/\text{CC}$ prepared by different cathodic current densities (A) 0; (B) -8 mA/cm^2 ; (C) -10 mA/cm^2 ; (D) -12 mA/cm^2 ; (E) -14 mA/cm^2 ; (F) -16 mA/cm^2 .

2.2.2. Photocurrent Response of $\text{WO}_3/\text{TiO}_2/\text{CC}$

In order to investigate the optimum separation efficiency of photoinduced electron–hole pairs for $\text{WO}_3/\text{TiO}_2/\text{CC}$, the photocurrent response was measured in 0.5 mol/L of the NaOH electrolyte without any sacrificial reagents. The nanomaterials were constructed by a constant cathodic current that changed from -8 mA/cm^2 to -16 mA/cm^2 . Chronoamperometry was used to test the photocurrent of the as-prepared materials with a time interval of 200 s and a voltage of $+0.245 \text{ V}$ (vs. RHE). Figure 3 showed the transient photocurrent generated under the illumination of visible light, and the maximum photocurrent density almost reached $60 \mu\text{A/cm}^2$. This is due to the increasing amount of WO_3 that served as active sites to improve the photocurrent. However, excessive WO_3 will reduce

the specific surface area. Hence, the optimal current density for the electrodeposition of $\text{WO}_3/\text{TiO}_2/\text{CC}$ nanocomposite is $-12 \text{ mA}/\text{cm}^2$.

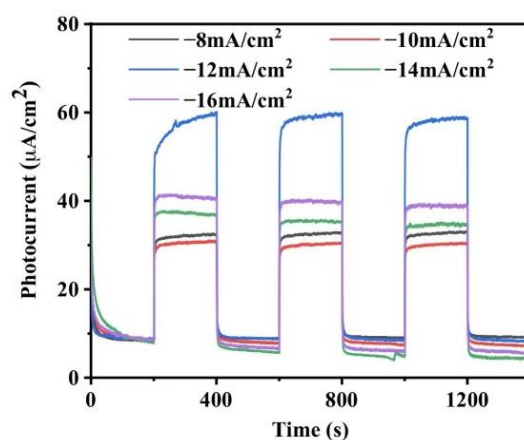


Figure 3. Photocurrent response diagram of $\text{WO}_3/\text{TiO}_2/\text{CC}$ materials prepared at different current densities under visible light irradiation.

2.3. SEM and Photocurrent Response of R- $\text{WO}_3/\text{R-TiO}_2/\text{CC}$

2.3.1. SEM Characterization

Figure 4A–F shows the SEM images of R- $\text{WO}_3/\text{R-TiO}_2/\text{CC}$ prepared by the reduction at different potentials. Apparently, the R- $\text{WO}_3/\text{R-TiO}_2/\text{CC}$ still maintains the rod-like morphology. With the increase in voltage reduction, the surface roughness is almost the same as that of $\text{WO}_3/\text{TiO}_2/\text{CC}$. Compared to $\text{WO}_3/\text{TiO}_2/\text{CC}$, the R- WO_3 film becomes thinner than the original WO_3 and more WO_3 is reduced at -1.355 V (vs. RHE). The formation of oxygen vacancies may be conducive to the separation and transmission of photogenerated electron–hole pairs, so as to improve the photocurrent.

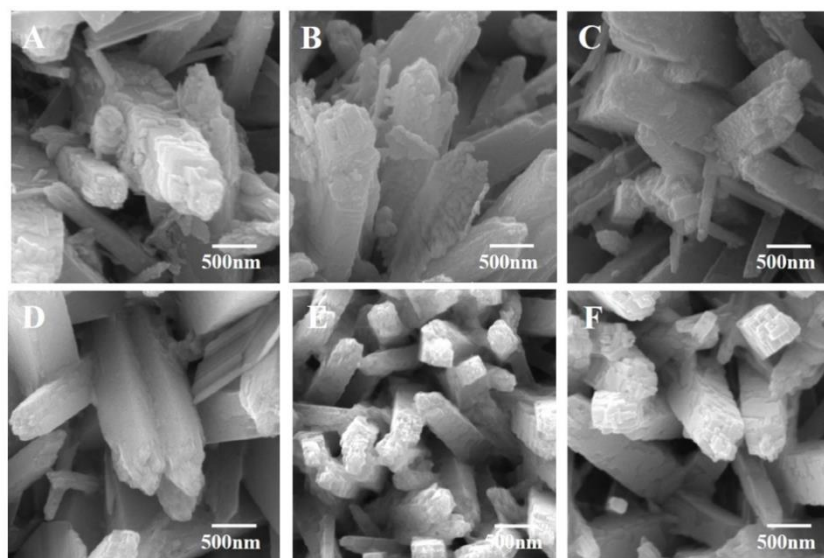


Figure 4. The SEM image of R- $\text{WO}_3/\text{R-TiO}_2/\text{CC}$ was prepared by electrochemical reduction of different potentials (A) -1.0 V ; (B) -1.2 V ; (C) -1.4 V ; (D) -1.6 V ; (E) -1.8 V ; (F) -2.0 V .

2.3.2. Photocurrent Response

The oxygen vacancies (O_{vs}) can affect the photoelectrochemical properties of nanocomposites. The photocurrent response test of R- $\text{WO}_3/\text{R-TiO}_2/\text{CC}$ was carried out by chronoamperometry at different voltages in 0.5 mol/L of the NaOH solution under visible light illumination, as shown in Figure 5A. With the increase in cathodic voltage from -1.0 V to

−1.6 V, the photocurrent density is remarkably enhanced with the peak value of about 160 $\mu\text{A}/\text{cm}^2$ under −1.6 V to prepare nanomaterials. This increase in photocurrent density is attributed to the generation of more O_{vs} at a high cathodic voltage, which is beneficial to the separation of photoinduced charge carriers. However, when the voltage exceeds −1.6 V, the photocurrent density begins to decay. In comparison, the photocurrent density of $\text{R-WO}_3/\text{R-TiO}_2/\text{CC}$ is dramatically higher than that of $\text{WO}_3/\text{TiO}_2/\text{CC}$, which indicates the electrochemical reduction of WO_3 promoted the photogenerated electron–hole pairs in the visible region.

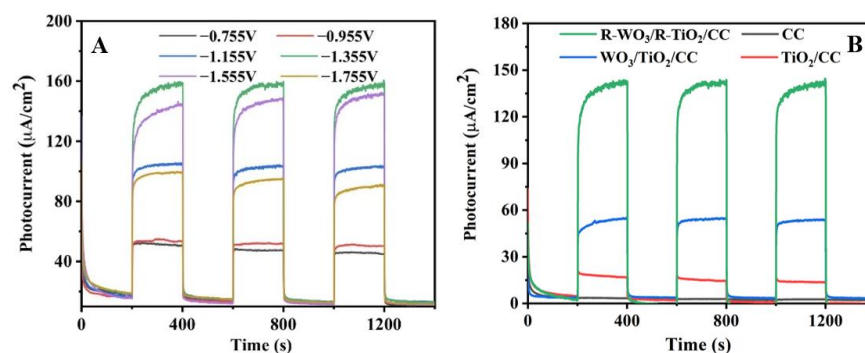
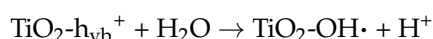
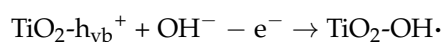
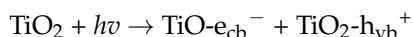


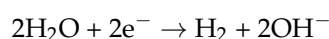
Figure 5. Comparison of photocurrent responses of $\text{R-WO}_3/\text{R-TiO}_2/\text{CC}$ under visible light irradiation at different cathodic voltages (vs. RHE) (A) and different nanomaterials (B).

Figure 5B shows the comparison of the photocurrent response for CC, TiO_2/CC , $\text{WO}_3/\text{TiO}_2/\text{CC}$, and $\text{R-WO}_3/\text{R-TiO}_2/\text{CC}$. The flexible CC shows a horizontal line, suggesting no photo response. The photocurrent of TiO_2/CC and $\text{WO}_3/\text{TiO}_2/\text{CC}$ is 20 $\mu\text{A}/\text{cm}^2$ and 54 $\mu\text{A}/\text{cm}^2$, respectively. Notably, the average photocurrent of $\text{R-WO}_3/\text{R-TiO}_2/\text{CC}$ is up to 142 $\mu\text{A}/\text{cm}^2$, which is 7.1 and 2.6 times higher than that of TiO_2/CC and $\text{WO}_3/\text{TiO}_2/\text{CC}$. It proves that the oxygen vacancy (O_{vs}) can enhance the charge transfer and separation, thus improving the photocatalytic performance. In an alkaline solution, photogenerated holes migrate to the anode surface and accumulate gradually under visible light irradiation. At the same time, OH^- ions are adsorbed on the electrode surface, so photogenerated holes and OH^- ions will undergo an oxidation reaction. OH^- ions lose electrons and form hydroxyl radicals, and then the positive photocurrent will flow in the external circuit. The general reactions may be as follows:

Photoanode:



Cathode (counter electrode):



where e^- and h^+ denote the photogenerated electron and hole, and the subscripts vb and cb represent the valence band and conduction band of TiO_2 , respectively.

2.3.3. TEM Characterization

$\text{R-WO}_3/\text{R-TiO}_2/\text{CC}$ and $\text{WO}_3/\text{TiO}_2/\text{CC}$ nanomaterials under optimal experimental conditions were tested by a transmission electron microscope (TEM). It can be seen from Figure 6A that the thickness of WO_3 loaded on the surface of TiO_2 is about 13 nm, and some nanoparticles (red dotted line) were deposited on the outermost layer (Figure 6B). The lattice fringes, with a spacing of 0.362 nm, corresponded to the (200) plane of WO_3 , which is evidenced by XRD. In contrast, the electrochemically reduced treatment of $\text{R-WO}_3/\text{R-TiO}_2/\text{CC}$ maintained the basic morphology of the nanorod (Figure 6C). The thickness

of R-WO₃ decreased, which was approximately 3 nm. The experiment results show that a constant cathode voltage reduction will narrow the thickness of R-WO₃, which may be due to the escape of hydrogen bubbles, resulting in the exfoliation of WO₃. Moreover, the nanocomposites exhibited an irregular lattice of WO₃ due to the formation of oxygen vacancies (Figure 6D). Moreover, both WO₃ and TiO₂ were reduced concurrently, which possibly produced low valance W⁵⁺ and Ti³⁺ in the process of the cathodic potential reduction.

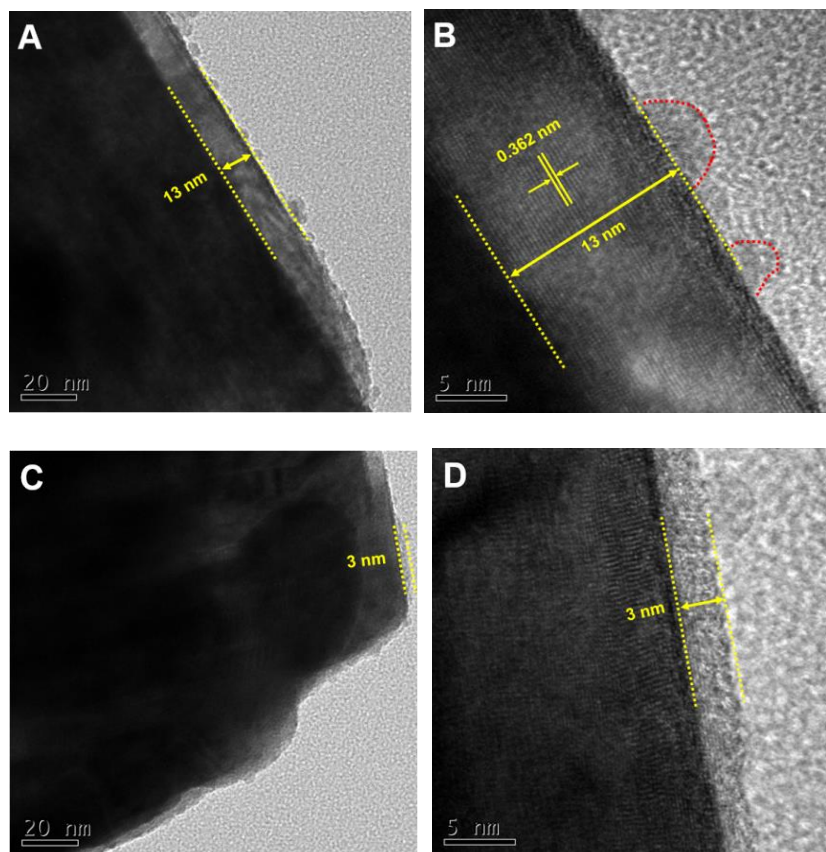


Figure 6. TEM and HR-TEM of WO₃/TiO₂/CC (A,B) and R-WO₃/R-TiO₂/CC (C,D).

2.3.4. XPS Analysis

The surface composition and valence states of nanomaterials were further investigated by X-ray photoelectron spectroscopy (XPS). The XPS survey spectra in Figure 7A showed that both R-WO₃/R-TiO₂/CC and WO₃/TiO₂/CC contain W, Ti, C, and O elements. The C 1s peaks of both samples originated from the carbon cloth. According to the high-resolution XPS spectrum, the reduced nanomaterials exhibited two characteristic peaks at 35.5 eV and 37.6 eV attributed to the peaks of W 4f_{7/2} and W 4f_{5/2}, respectively. In addition, the Ti 2p XPS spectra of both nanomaterials displayed two obvious peaks at 458.9 eV and 464.2 eV corresponding to the characteristic peaks of Ti 2p_{3/2} and Ti 2p_{1/2}. Compared to the original WO₃/TiO₂/CC, the self-doped R-WO₃/R-TiO₂/CC exhibited a negative shift for binding energy for the peaks of W 4f and Ti 2p.

The XPS spectra of W 4f could be deconvoluted into two corresponding doublets, W⁶⁺ and W⁵⁺. In addition, it can be seen that Ti 2p included two valence states of Ti³⁺ and Ti⁴⁺, indicating both WO₃ and TiO₂ can be reduced simultaneously, which is consistent with the results of HR-TEM analysis. The experimental results strongly prove that the electrochemical method of cathode voltage reduction can form oxygen vacancies.

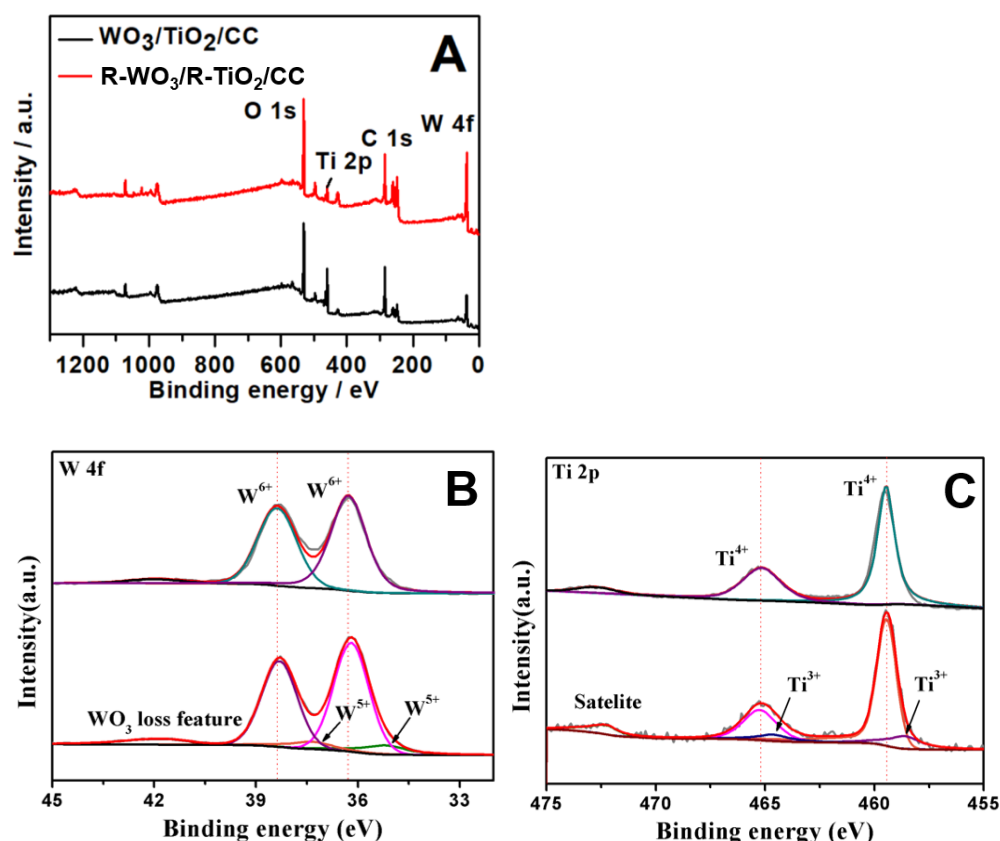


Figure 7. The XPS survey spectra (A), high-resolution XPS spectra of W 4f (B) and Ti 2p (C).

2.4. Optical Properties and Energy Band Structure of Materials

2.4.1. Optical Properties

Figure 8A shows the ultraviolet-visible diffuse reflection spectrum (DRS) of WO₃, WO₃/CC, TiO₂/CC, and R-WO₃/R-TiO₂/CC materials. It can be observed that TiO₂/CC has a strong absorption under ultraviolet light, but the absorption is extremely small under visible light; pure WO₃ has an absorption in the visible region with a wavelength of less than 480 nm. Compared with WO₃/CC, the absorption in the visible region has a significant red shift, which may be caused by the absorption of visible light by the carbon fiber cloth. In contrast, R-WO₃/R-TiO₂/CC presents an obvious absorption in the visible light region, and its absorption band edge reaches about 650 nm, which broadens the spectral response range. For sunlight, ultraviolet light only accounts for about 5%, while visible light accounts for 43%. When TiO₂ and reduced WO₃ are combined in R-WO₃/R-TiO₂/CC, the absorption wavelength of light can extend into the visible light range, thus improving the effective utilization rate of light and photocatalytic performance.

The Tauc plot (Figure 8B) can be converted by UV-Vis DRS, and the semiconductor band gap width can be calculated by the following formula:

$$(\alpha h\nu)^{1/n} = A(h\nu - E_g) \quad (1)$$

where α is the absorbance index, h is the Planck constant, ν is the frequency, E_g is the band gap of the semiconductor, and A and n are constants. When n is 1/2 or 2, the nanomaterial is a semiconductor of direct or indirect electronic transition in the band gap, respectively [39]. According to formula (1), taking $(\alpha h\nu)^{1/n}$ as ordinate and $h\nu$ as abscissa, the Tauc plot can be obtained, as depicted in Figure 6B. The intersection of the TiO₂ curve for the tangent and abscissa is 3.0 eV, i.e., the band gap of the TiO₂ material is 3.0 eV, which is consistent with the XRD of rutile TiO₂ [40]. Moreover, the band gap of WO₃ is 2.46 eV, which suggests that WO₃ can diminish the forbidden band width of nanocomposite [40].

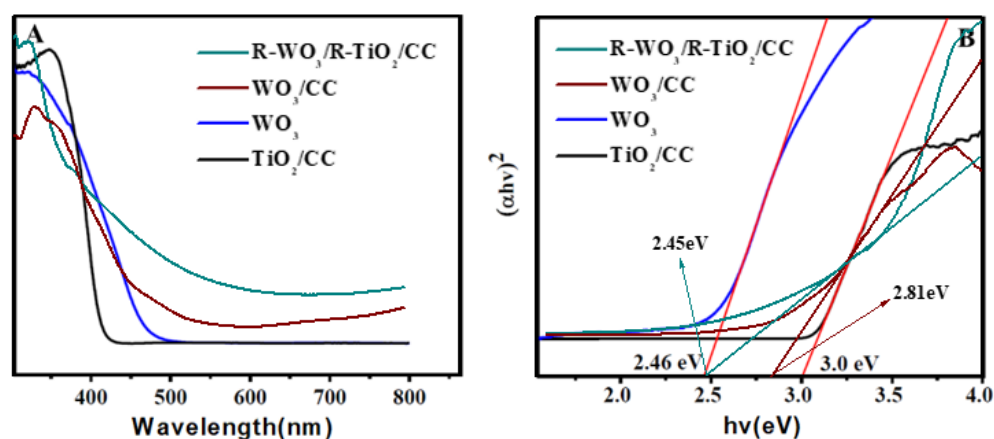


Figure 8. UV-visible DRS of TiO₂/CC and R-WO₃/R-TiO₂/CC (A) and Tauc plot (B).

2.4.2. Energy Level Structure

The positions of the valence band (VB) and the conduction band (CB) of nanomaterials can be computed by the following empirical formulas:

$$E_{VB} = X - E^e + 1/2E_g \quad (2)$$

$$E_{CB} = E_{VB} - E_g \quad (3)$$

where E_{VB} is the VB potential, E^e is the electron energy (usually 4.5 eV), E_{CB} is the CB potential, E_g is the band gap width, and X is the absolute electronegativity of the TiO₂ and WO₃ semiconductor, which can be calculated by the geometric average electronegativity of each atom of the compound by the following formula.

$$G_n = \sqrt[n]{\prod_{i=1}^n x_i^{f_i}} = \sqrt[n]{x_1^{f_1} x_2^{f_2} x_3^{f_3} \dots x_n^{f_n}} \quad (4)$$

where G_n is the geometric average electronegativity, x_i is the electronegativity, and f_i is the number of atoms in the compounds.

The electronegativity of the Ti atom, O atom, and W atom is 3.45 eV, 7.54 eV, and 4.40 eV, respectively [41]. Therefore, the absolute electronegativity of TiO₂ and WO₃ is 5.81 eV and 6.59 eV. According to formulas (2) and (3) above, the VB position of TiO₂ is 2.81 eV and the CB position is −0.19 eV. Correspondingly, the VB position of WO₃ is 3.32 eV and the CB position is 0.86 eV. It can be concluded that the photogenerated holes will transfer from TiO₂ to WO₃ because the VB of TiO₂ is higher than that of WO₃, which will improve the separation efficiency of photoinduced charge carriers.

2.5. Electrochemical Properties

2.5.1. Electrochemical Impedance Spectroscopy

In order to investigate of electron transfer across the interface between nanomaterials and the electrolyte, electrochemical impedance spectroscopy (EIS) is a useful technology that can provide information regarding the resistance and capacitance. As shown in Figure 9, the three nanomaterials exhibit similar semicircles dominated by charge transfer in the Nyquist complex plane with a potential of +0.445 V (vs. RHE) under visible light irradiation. Compared with TiO₂/CC and WO₃/TiO₂/CC, the Nyquist graph of R-WO₃/R-TiO₂/CC displays that its semicircle corresponds to a smaller diameter, indicating that the impedance of charge transfer is smaller and can more easily conduct electrons.

The equivalent circuit of different nanomaterials is also fitted under visible light irradiation depicted in Figure 9. The R_1 corresponds to the total resistance of the electrolyte and the metal oxides. R_2 is assigned to the impedance of charge transport in the nanomaterials. Compared to the solution resistance of TiO₂/CC, the 3.5 Ω of R-WO₃/R-TiO₂/CC is

much smaller than $4.3\ \Omega$ of TiO_2/CC . Similarly, the solution resistance of $\text{WO}_3/\text{TiO}_2/\text{CC}$ decreases. Moreover, the charge resistance changes from $215\ \Omega$ of TiO_2/CC to $205\ \Omega$ of $\text{R-WO}_3/\text{R-TiO}_2/\text{CC}$, indicating faster ion and electron transport [41]. Clearly, R-WO_3 with high conductivity can boost electron transfer during the electrochemical reaction. This is conducive to the rapid transfer of the photogenerated electrons to the external circuit and the prevention of the recombination of photogenerated charge carriers.

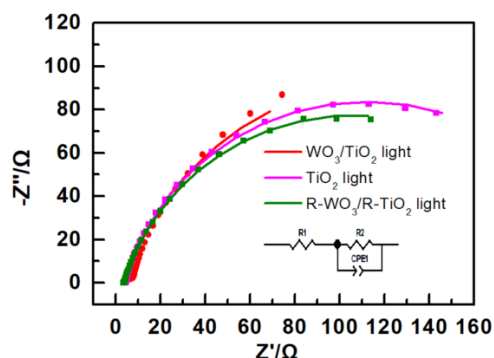


Figure 9. EIS of TiO_2/CC , $\text{WO}_3/\text{TiO}_2/\text{CC}$, and $\text{R-WO}_3/\text{R-TiO}_2/\text{CC}$ materials under sunlight irradiation.

2.5.2. Mott-Schottky Test

The donor density and flat band potential of the semiconductor were studied by the Mott–Schottky (M–S) method. Figure 10 shows the M–S curves of TiO_2/CC and $\text{R-WO}_3/\text{R-TiO}_2/\text{CC}$. The slope of TiO_2/CC is positive, indicating TiO_2 is an n-type semiconductor. In comparison, the type of the WO_3 semiconductor can be converted from n-type to p-type under the applied electric field, that is, the slope of the $\text{R-WO}_3/\text{R-TiO}_2/\text{CC}$ composite material is positive between $-1.3\ \text{V}$ and $-1.0\ \text{V}$, while the slope is negative when the voltage is between $-0.9\ \text{V}$ and $-0.7\ \text{V}$.

The donor density is calculated by the following formula [31]:

$$C^{-2} = \frac{2}{e\epsilon_0\epsilon_r N_d} \left(E - E_{FB} - \frac{kT}{e} \right) \quad (5)$$

where C is the capacitance of space charge layer, e is the electronic charge ($e = 1.602 \times 10^{-19}\ \text{C}$), ϵ_0 is the vacuum dielectric constant ($\epsilon_0 = 8.854 \times 10^{-14}\ \text{F}\cdot\text{cm}^{-1}$), ϵ_r is the relative dielectric constant of a material, k is the Boltzmann constant ($1.381 \times 10^{-23}\ \text{J}\cdot\text{K}^{-1}$), T is the absolute temperature, E is the electrode potential, E_{FB} is the flat band potential, and N_d is the donor carrier density. When C^{-2} is zero, the intersection point is equivalent to the flat band potential (E_{FB}), which is found to be $-1.25\ \text{V}$ for $\text{R-WO}_3/\text{R-TiO}_2/\text{CC}$. The value of E_{FB} drifted negatively to $-0.3\ \text{V}$ compared to that of the TiO_2/CC nanomaterials.

Since kT/e at room temperature is approximately $25\ \text{mV}$, which can be negligible, we can obtain the formula as follows:

$$N_d = \frac{2}{e\epsilon_0\epsilon_r} \left[\frac{d(C^{-2})}{dE} \right]^{-1} \quad (6)$$

According to the above formula (6), supposing that ϵ_r is known for most of the semiconductors, the N_d of the nanocomposite can be calculated from the tangent slope and the ϵ_r of the nanomaterials.

From Figure 10, the E_{FB} of TiO_2/CC is $-0.95\ \text{V}$. Furthermore, considering that reduced WO_3 has a more negative charge, R-WO_3 represents an n-type semiconductor, hence $-1.25\ \text{V}$ of E_{FB} for $\text{WO}_3/\text{TiO}_2/\text{CC}$ is chosen. Compared with TiO_2/CC , the flat band potential of $\text{R-WO}_3/\text{R-TiO}_2/\text{CC}$ is negatively shifted by $0.30\ \text{V}$, which suggests an increase in the semiconductor Fermi level. Subsequently, the semiconductor conduction band also shifts negatively, the energy level of electrons becomes higher and more unstable, and the

electrons in the conduction band are more easily lost and undergo an oxidation reaction. For the solution, the particles in the solution obtain the electrons on the semiconductor conduction band and undergo the photoreduction reaction more easily. From the thermodynamic point of view, the more negative flat band potential of the nanocomposites implies that the electrons excited on the conduction band after irradiation have a stronger reduction ability.

Assuming that the ϵ of TiO_2 is 110, as reported in the literature [15], the N_d of TiO_2/CC is $4.27 \times 10^{22} \text{ cm}^{-3}$.

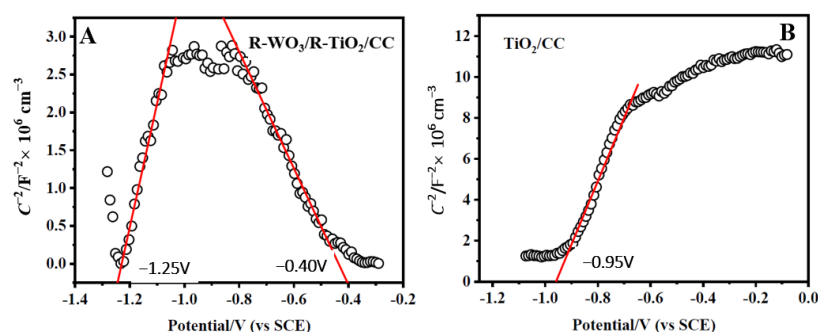


Figure 10. Mott-Schottky (M-S) of $\text{R-WO}_3/\text{R-TiO}_2/\text{CC}$ (A) and TiO_2/CC (B) with 5000 Hz of frequency at 10 mV of amplitude.

2.6. Photocatalytic Activity Analysis

Figure 11A shows the photocatalytic degradation of the methylene blue (MB) pollutant under visible light with a 420 nm cutoff filter with different photocatalysts. The degradation rate after illumination is calculated according to the following formula:

$$\text{The degradation rate} = \frac{A_0 - A_t}{A_0} \times 100\% \quad (7)$$

where A_0 and A_t are the absorbances of methylene blue solution for 0 min and t min, respectively.

After 3 h of visible light irradiation for the carbon cloth, the photocatalytic degradation rate of MB is only 15%, which is due to the photolysis. The MB degradation rate for TiO_2/CC and $\text{WO}_3/\text{TiO}_2/\text{CC}$ is about 31% and 56%, respectively. Notably, the degradation rate for $\text{R-WO}_3/\text{R-TiO}_2/\text{CC}$ is 68%. These results demonstrate the improvement of the photocatalytic activity when the nanocomposites are utilized. Among them, $\text{R-WO}_3/\text{R-TiO}_2/\text{CC}$ exhibits the highest photocatalytic degradation rate due to the narrow band gap of WO_3 , which enlarges the light response range and hinders the recombination of photogenerated electron-hole pairs, thus enhancing the charge transport and separation and improving the photocatalytic performance.

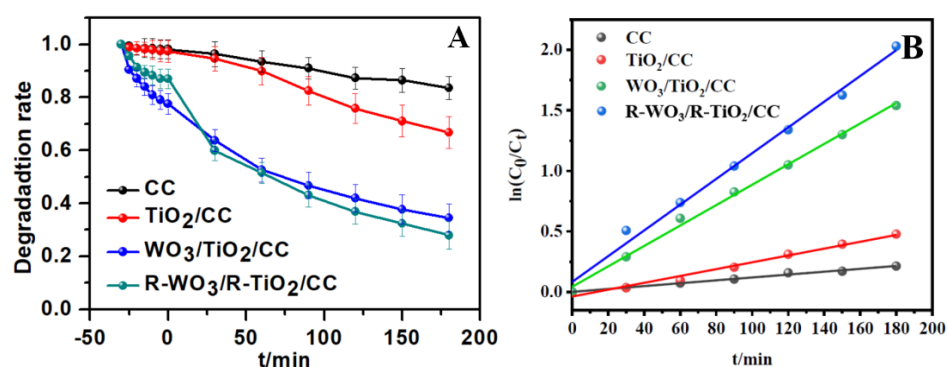


Figure 11. Photocatalytic degradation of the different composites with error bars (A) and pseudo-first-order kinetic curve (B).

Figure 11B shows the quasi-first-order kinetic curves of the photocatalytic degradation rate for CC, TiO₂/CC, WO₃/TiO₂/CC, and R-WO₃/R-TiO₂/CC. The equation can be gained by the least-square method for curve fitting. According to the fitting curve, the degradation rate constant k of the above materials is 0.01063 min⁻¹, 0.00843 min⁻¹, 0.00282 min⁻¹, and 0.00119 min⁻¹, respectively. The rate constant k of R-WO₃/R-TiO₂/CC composites is 1.3 times and 3.8 times that of WO₃/TiO₂/CC and TiO₂/CC composites, as shown in Table 1.

Table 1. Equation of quasi-first-order dynamics.

The Sample	Kinetic Equation
CC	$Y = 0.00183 + 0.00119 X$
TiO ₂ /CC	$Y = -0.03657 + 0.00282 X$
WO ₃ /TiO ₂ /CC	$Y = 0.04365 + 0.00843 X$
R-WO ₃ /R-TiO ₂ /CC	$Y = 0.08403 + 0.01063 X$

2.7. Photocatalytic Mechanism Analysis

Figure 12 shows the photocatalytic mechanism of R-WO₃/R-TiO₂/CC for MB degradation under visible light irradiation. According to the relative position of the semiconductor VB and CB, the CB of WO₃ is lower than that of TiO₂, and the excited state electrons of TiO₂ will be spontaneously injected into the CB of WO₃, thus WO₃ acts as an acceptor for the photogenerated electron. Meanwhile, the VB of WO₃ is higher than that of TiO₂, and the photogenerated holes of WO₃ will readily transfer to the VB of TiO₂ [42]. Later, O₂ can be scavenged by electrons to yield O₂^{•-}. In the meantime, OH⁻ can react with holes to produce OH•. Both O₂^{•-} and OH• as active species are able to oxidize MB, achieving the purpose of degradation [43].

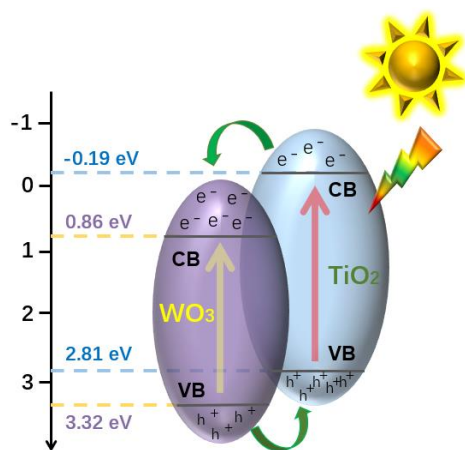


Figure 12. Schematic diagram of photocatalysis in the R-WO₃/R-TiO₂/CC nanocomposite.

3. Experimental

3.1. Materials and Characterizations

Carbon cloth was purchased from Shanghai Three Musk Deer Industry Co., Ltd., (Shanghai, China). Tetrabutyl titanate, sodium tungstate, ammonium acetate, and methylene blue were purchased from Aladdin Bio-Chem Technology Co., Ltd., (Shanghai, China). All other reagents were of analytical grade and used without further purification. Deionized water (>18.4 MΩ cm⁻¹) was used for all solution preparations. The photoelectrochemical measurements were performed in Na₂SO₄ or NaOH electrolytes.

The X-ray diffraction pattern (XRD) was measured with a Bruker D8 Advance diffractometer (Karlsruhe, Germany). Scanning electron microscopy (SEM) was determined by a MIRA3 LMU microscope (Brno, Czech Republic) at 15.0 kV. The transmission electron microscopy (TEM) was measured with FEI Tecnai F20 (Hillsboro, OR, USA). the X-ray pho-

photoelectron spectroscopy (XPS) was detected by the ESCALAB 250Xi (Waltham, MA, USA). The UV-Vis diffuse reflectance spectrum (DRS) was tested by the UV2600 spectrophotometer (Shimadzu, Japan). The photoelectrochemical performance was measured by the CS electrochemical workstation (Wuhan Corrtest Instrument Corp., Ltd., Wuhan, China). Light intensity is measured with an irradiatometer (Model: FZ-A) purchased from Beijing Normal University Photoelectric Instrument Factory (Beijing, China). The three-electrode system was established with R-WO₃/TiO₂/CC as the working electrode, a saturated calomel electrode (SCE) as the reference electrode, and Pt foil as the auxiliary electrode.

3.2. The Preparation of TiO₂/CC Nanomaterials

TiO₂ was prepared on carbon cloth (CC) by hydrothermal method. Firstly, the CC was immersed for ultrasonic cleaning for 10 min in acetone, ethanol, and distilled water. Subsequently, the CC was dried at 60 °C and calcined at 500 °C for 5 h in a tube furnace. Next, 30 mL of concentrated hydrochloric acid was slowly poured into 30 mL of distilled water under agitation. Then 1.5 mL of the tetrabutyl titanate solution was dropped into the hydrochloric acid solution with a pipette, which was stirred for 15 min. Finally, the pretreated CC was placed into the 50 mL Teflon-lined stainless-steel autoclave and the above solution was added to initiate the deposition at 150 °C for 15 h. After the reaction was completed and cooled to an ambient temperature, the CC was taken out and washed with distilled water, and then dried in a 60 °C oven to obtain the TiO₂/CC material.

3.3. The Preparation of WO₃/TiO₂/CC Nanomaterials

WO₃ was coated on TiO₂/CC by the electrochemical deposition method. Ethylenediaminetetraacetic acid (EDTA), Na₂WO₄, and CH₃COONH₄ were accurately weighed and dissolved to prepare a mixed solution with a concentration of 0.30 mol/L. The three-electrode system was constructed by TiO₂/CC, platinum foil, and SCE, which were used as the working electrode, counter electrode, and reference electrode, respectively. The immersion area of the TiO₂/CC electrode was 1 cm × 2 cm in the above mixed solution, and then the electrochemical deposition was carried out for 10 min under the cathodic current from −8 mA/cm² to −16 mA/cm², and dried in an oven to obtain WO₃/TiO₂/CC. Finally, the WO₃/TiO₂/CC was annealed at 450 °C for 2 h.

3.4. The Fabrication of R-WO₃/TiO₂/CC Nanomaterials

The R-WO₃/TiO₂/CC was fabricated via an electrochemical reduction. In a typical experiment, WO₃/TiO₂/CC, a platinum sheet electrode, and saturated calomel (SCE) were immersed in 0.1 mol/L of a Na₂SO₄ solution with an area of 1 cm × 2 cm. The cathodic voltage varied from −0.755 V to −1.755 V (vs. RHE) for 10 min. After the electrochemical reduction, the composite material was rinsed and then dried at 60 °C. Finally, the optimum conditions of R-WO₃/TiO₂/CC were determined by a photoelectrochemical performance test and SEM analysis.

3.5. Photocatalytic Performance Test

The photocatalytic performance was tested by analyzing the degradation rate of the methylene blue (MB) solution as the target pollutant under the irradiation of a 300 W xenon lamp with a 420 nm cutoff filter. Then, 5 mg/L of the MB in a 50 mL solution was loaded in a double-layer quartz beaker. Three 2 cm × 1 cm nanocomposites were placed side by side in the center of the solution. Before the start of degradation, the pollutant solution was placed in dark conditions for 30 min to achieve the equilibrium of adsorption-desorption with the nanocomposites. Subsequently, the light intensity was adjusted to AM 1.5 G (100 mW/cm²) to irradiate the MB solution. During the degradation process, the solution was measured every 30 min until the end of the reaction. The relationship between concentration and absorbance was $C_t/C_0 = A_t/A_0$. The absorbance was examined at 664 nm using a visible spectrophotometer.

3.6. The Measurement of Photoelectrochemical Properties

The photochemical properties of the as-prepared materials were tested using a three-electrode system in 0.5 mol/L of the NaOH electrolyte. A xenon lamp was used as the simulated light source, and the photocurrent response of the materials was tested by the chronoamperometry method of an electrochemical workstation under +0.425 V (vs. RHE). In addition, electrochemical impedance spectroscopy (EIS) for the nanomaterials was at a frequency range of 100 kHz to 0.01 Hz in 0.5 mol/L NaOH with +0.425 V and a 5 mV amplitude. The Mott–Schottky (M–S) test with a frequency of 5000 Hz at 10 mV of amplitude was carried out to further calculate the carrier density of the nanomaterials in 0.5 mol/L of the Na₂SO₄ solution.

4. Conclusions

In summary, oxygen-deficient R-WO₃/R-TiO₂/CC photocatalytic nanomaterial with a three-dimensional structure was successfully prepared on flexible carbon cloth by hydrothermal and electrochemical methods. The electrodeposited WO₃ was able to narrow the energy gap of the nanocomposite, promoting the absorption of visible light. Moreover, reduced WO₃ produced oxygen vacancies, which reduced the resistance of the solution and the charge transfer, thus enhancing the photocurrent density up to 142 $\mu\text{A}/\text{cm}^2$. The results indicated that the reduced WO₃ further improved the separation efficiency of photoinduced charge carriers to impede the recombination of electrons and holes. More importantly, the as-prepared nanomaterials were used to degrade the MB under visible light irradiation. The degradation rate of R-WO₃/R-TiO₂/CC was 68%, higher than that of WO₃/TiO₂/CC (56%) and TiO₂/CC (31%), which reflected the fact that the formation of heterojunction microstructure prolonged the lifetime of photogenerated electron–hole pairs between WO₃ and TiO₂, thus increasing the photocatalytic activity. This study provides new insight into the development of nanocomposite photocatalysts with visible light activity.

Author Contributions: L.J.: Conceptualization, investigation, resources, writing—original draft. X.G.: Conceptualization, investigation, resources, writing—original draft. S.C.: Conceptualization, investigation, formal analysis. J.A.: Writing—review and editing. S.K.: Funding acquisition, resources, project administration, supervision, validation. All authors have read and agreed to the published version of the manuscript.

Funding: Ministry of Education, T2, Singapore: WBS: R279-000-544-112; FRC MOE T1 project (R-279-000-632-114); GEP project (R-279-000-553-731); LCER FI project (LCERFI 01-0023); Guangzhou Basic and Applied Basic Research Project in China: 202102020134; Youth Innovation Talents Project of Guangdong Universities (natural science): 2019KQNCX098; Natural Science Foundation of Guangdong Province: 2015A030313841; Foundation for Distinguished Young Talents in Higher Education of Guangdong: 2012LYM_0099.

Data Availability Statement: All data included in this study are available upon permission from the publishers.

Acknowledgments: Generous acknowledgement is given to the Ministry of Education, T2, Singapore: WBS: R279-000-544-112; FRC MOE T1 project (R-279-000-632-114); GEP project (R-279-000-553-731); LCER FI project (LCERFI 01-0023); Guangzhou Basic and Applied Basic Research Project in China: 202102020134; Youth Innovation Talents Project of Guangdong Universities (natural science): 2019KQNCX098; Natural Science Foundation of Guangdong Province: 2015A030313841; Foundation for Distinguished Young Talents in Higher Education of Guangdong: 2012LYM_0099.

Conflicts of Interest: The authors declare no conflict of interest.

References

1. Zhu, S.; Wang, D. Photocatalysis: Basic Principles, Diverse Forms of Implementations and Emerging Scientific Opportunities. *Adv. Energy Mater.* **2017**, *7*, 1700841. [[CrossRef](#)]
2. Chu, Z.; Qiu, L.; Chen, Y.; Zhuang, Z.; Du, P.; Xiong, J. TiO₂-loaded carbon fiber: Microwave hydrothermal synthesis and photocatalytic activity under UV light irradiation. *J. Phys. Chem. Solids* **2020**, *136*, 109138. [[CrossRef](#)]

3. Zhou, F.; Ren, X.; Liu, J.; Liu, P. Development of Photocatalytic Degradation of Organic Pollutants in Water. *J. Mater. Eng.* **2018**, *46*, 9–19. [\[CrossRef\]](#)
4. Shayegan, Z.; Lee, C.-S.; Haghighat, F. TiO₂ photocatalyst for removal of volatile organic compounds in gas phase—a review. *Chem. Eng. J.* **2018**, *334*, 2408–2439. [\[CrossRef\]](#)
5. Shu, Y.; Ji, J.; Xu, Y.; Deng, J.; Huang, H.; He, M.; Leung, D.Y.C.; Wu, M.; Liu, S.; Liu, S.; et al. Promotional role of Mn doping on catalytic oxidation of VOCs over mesoporous TiO₂ under vacuum ultra-violet (VUV) irradiation. *Appl. Catal. B Environ.* **2018**, *220*, 78–87. [\[CrossRef\]](#)
6. Tung, M.H.T.; Cam, N.T.D.; Thuan, D.V.; Quan, P.V.; Hoang, C.V.; Phuong, T.T.T.; Lam, N.T.; Tam, T.T.; Chi, N.T.P.L.; Lan, N.T.; et al. Novel direct Z-scheme AgI/N-TiO₂ photo catalyst for removal of polluted tetracycline under visible irradiation. *Ceram. Int.* **2020**, *46*, 6012–6021. [\[CrossRef\]](#)
7. Zhang, W.; He, H.; Tian, Y.; Lan, K.; Liu, Q.; Wang, C.; Liu, Y.; Elzatahry, A.; Che, R.; Li, W.; et al. Synthesis of uniform ordered mesoporous TiO₂ microspheres with controllable phase junctions for efficient solar water splitting. *Chem. Sci.* **2019**, *10*, 1664–1670. [\[CrossRef\]](#)
8. Zhang, P.; Lu, X.; Luan, D.; Lou, X. Fabrication of Heterostructured Fe₂TiO₅-TiO₂ Nan cages with Enhanced Photo electrochemical Performance for Solar Energy Conversion. *Angew. Chem. Int. Ed.* **2020**, *59*, 8128–8132. [\[CrossRef\]](#)
9. Kuang, Y.; Jia, Q.; Ma, G.; Hisatomi, T.; Minegishi, T.; Nishiyama, H.; Nakabayashi, M.; Shibata, N.; Yamada, T.; Kudo, A.; et al. Ultrastable low-bias water splitting photoanodes via photocorrosion inhibition and in situ catalyst regeneration. *Nat. Energy* **2017**, *2*, 16191. [\[CrossRef\]](#)
10. Kocijan, M.; Ćurković, L.; Radošević, T.; Podlogar, M. Enhanced Photocatalytic Activity of Hybrid rGO@TiO₂/CN Nanocomposite for Organic Pollutant Degradation under Solar Light Irradiation. *Catalysts* **2021**, *11*, 1023. [\[CrossRef\]](#)
11. Schwarze, M.; Klingbeil, C.; Do, H.U.; Kutorglo, E.M.; Parapat, R.Y.; Tasbihi, M. Highly Active TiO₂ Photocatalysts for Hydrogen Production through a Combination of Commercial TiO₂ Material Selection and Platinum Co-Catalyst Deposition Using a Colloidal Approach with Green Reductants. *Catalysts* **2021**, *11*, 1027. [\[CrossRef\]](#)
12. Kim, S.; Chang, H.-K.; Kim, K.B.; Kim, H.-J.; Lee, H.-N.; Park, T.J.; Park, Y.M. Highly Porous SnO₂/TiO₂ Heterojunction Thin-Film Photocatalyst Using Gas-Flow Thermal Evaporation and Atomic Layer Deposition. *Catalysts* **2021**, *11*, 1144. [\[CrossRef\]](#)
13. Cui, Z.; Sun, Y.; Zhang, Z.; Xu, M.; Xin, B. Facile synthesis and photocatalytic activity of Ag₃PO₄ decorated MoS₂ nano flakes on carbon fiber cloth. *Mater. Res. Bull.* **2018**, *100*, 345–352. [\[CrossRef\]](#)
14. Wu, N.; Wang, Y.; Lei, Y.; Wang, B.; Han, C. Flexible N-doped TiO₂/C ultrafine fiber mat and its photocatalytic activity under simulated sunlight. *Appl. Surf. Sci.* **2014**, *319*, 136–142. [\[CrossRef\]](#)
15. Yen, L.T.H.; Thuan, D.V.; Hanh, N.T.; Vy, N.H.T.; Hang, T.T.M.; Ha, H.V.; Pham, T.-D.; Sharma, A.K.; Nguyen, M.V.; Dang N.-M.; et al. Synthesis of N and S Co-doped TiO₂ Nanotubes for Advanced Photocatalytic Degradation of Volatile Organic Compounds (VOCs) in Gas Phase. *Top. Catal.* **2020**, *63*, 1077–1085.
16. Ding, X.; Liu, H.; Chen, J.; Wen, M.; Li, G.; An, T.; Zhao, H. In situ growth of well-aligned Ni-MOF nan sheets on nickel foam for enhanced photocatalytic degradation of typical volatile organic compounds. *Nanoscale* **2020**, *12*, 9462–9470. [\[CrossRef\]](#) [\[PubMed\]](#)
17. Li, J.; Cai, L.; Shang, J.; Yu, Y.; Zhang, L. Giant enhancement of internal electric field boosting bulk charge separation for photocatalysis. *Adv. Mater.* **2016**, *28*, 4059–4064. [\[CrossRef\]](#)
18. Sharma, A.; Lee, B.K. Photocatalytic reduction of carbon dioxide to methanol using nickel-loaded TiO₂ supported on activated carbon fiber. *Catal. Today* **2017**, *298*, 158–167. [\[CrossRef\]](#)
19. Xu, H.; Zhang, L. Controllable one-pot synthesis and enhanced visible light photocatalytic activity of tunable C-Cl-codoped TiO₂ nanocrystals with high surface area. *J. Phys. Chem. C* **2010**, *114*, 940–946. [\[CrossRef\]](#)
20. Sood, S.; Umar, A.; Mehta, S.K.; Kansal, S.K. Highly effective Fe-doped TiO₂ Nanoparticles photocatalysts for visible-light driven photocatalytic degradation of toxic organic compounds. *J. Colloid Interf. Sci.* **2015**, *450*, 213–223. [\[CrossRef\]](#)
21. Lv, J.; Gao, H.; Wang, H.; Lu, X.; Xu, G.; Wang, D.; Chen, Z.; Zhang, X.; Zheng, Z.; Wu, Y. Controlled deposition and enhanced visible light photocatalytic performance of Pt-modified TiO₂ nanotube arrays. *Appl. Surf. Sci.* **2015**, *351*, 225–231. [\[CrossRef\]](#)
22. Wang, Y.; Zhu, S.; Chen, X.; Tang, Y.; Jiang, Y.; Peng, Z.; Wang, H. One-step template-free fabrication of mesoporous ZnO/TiO₂ hollow microspheres with enhanced photocatalytic activity. *Appl. Surf. Sci.* **2014**, *307*, 263–271. [\[CrossRef\]](#)
23. Wang, X.; Sun, M.; Murugananthan, M.; Zhang, Y.; Zhang, L. Electrochemically self-doped WO₃/TiO₂ nanotubes for photocatalytic degradation of volatile organic compounds. *Appl. Catal. B Environ.* **2020**, *260*, 118205. [\[CrossRef\]](#)
24. Theerthagiri, J.; Chandrasekaran, S.; Salla, S.; Elakkiya, V.; Senthil, R.A.; Nithyadharseni, P.; Maiyalagan, T.; Micheal, K.; Ayeshamariam, A.; Arasu, M.V.; et al. Recent developments of metal oxide based heterostructures for photocatalytic applications towards environmental remediation. *J. Solid State Chem.* **2018**, *267*, 35–52. [\[CrossRef\]](#)
25. Pinedo-Escobar, J.A.; Fan, J.; Moctezuma, E.; Gomez-Solis, C.; Martinez, C.J.C.; Gracia-Espino, E. Nanoparticulate Double-Heterojunction Photocatalysts Comprising TiO₂(Anatase)/WO₃/TiO₂(Rutile) with Enhanced Photocatalytic Activity toward the Degradation of Methyl Orange under Near-Ultraviolet and Visible Light. *ACS Omega* **2021**, *6*, 11840–11848. [\[CrossRef\]](#)
26. Jiang, D.; Otitoju, T.A.; Ouyang, Y.; Shoparwe, N.F.; Wang, S.; Zhang, A.; Li, S. A Review on Metal Ions Modified TiO₂ for Photocatalytic Degradation of Organic Pollutants. *Catalysts* **2021**, *11*, 1039. [\[CrossRef\]](#)
27. Garcia, R.M.; Carleer, R.; Pérez, M.A.; Torres, J.P.; Gu, Y.; Samyn, P.; Yperman, J. Fe-TiO₂/AC and Co-TiO₂/AC Composites: Novel Photocatalysts Prepared from Waste Streams for the Efficient Removal and Photocatalytic Degradation of Cibacron Yellow F-4G Dye. *Catalysts* **2021**, *11*, 1037.

28. Iqbal, A.; Saidu, U.; Sreekantan, S.; Ahmad, M.N.; Rashid, M.; Ahmed, N.M.; Danial, W.H.; Wilson, L.D. Mesoporous TiO₂ Implanted ZnO QDs for the Photodegradation of Tetracycline: Material Design, Structural Characterization and Photodegradation Mechanism. *Catalysts* **2021**, *11*, 1205. [\[CrossRef\]](#)
29. Zhang, L.; Qin, M.; Yu, W.; Zhang, Q.; Xie, H.; Sun, Z.; Shao, Q.; Guo, X.; Hao, L.; Zheng, Y.; et al. Heterostructured TiO₂/WO₃ Nanocomposites for Photocatalytic Degradation of Toluene under Visible Light. *J. Electrochem. Soci.* **2017**, *164*, H1086–H1090. [\[CrossRef\]](#)
30. Smith, W.; Wolcott, A.; Fitzmorris, R.C.; Zhang, J.Z.; Zhao, Y. Quasi-core-shell TiO₂/WO₃ and WO₃/TiO₂ nanorod arrays fabricated by glancing angle deposition for solar water splitting. *J. Mater. Chem.* **2011**, *21*, 10792–10800. [\[CrossRef\]](#)
31. Joice, M.R.S.; David, T.M.; Wilson, P. WO₃ Nanorods Supported on Mesoporous TiO₂ Nanotubes as One-Dimensional Nanocomposites for Rapid Degradation of Methylene Blue under Visible Light Irradiation. *J. Phys. Chem. C* **2019**, *123*, 27448–27464. [\[CrossRef\]](#)
32. Odhiambo, V.O.; Ongarbayeva, A.; Kéri, O.; Simon, L.; Szilágyi, I.M. Synthesis of TiO₂/WO₃ Composite Nanofibers by a Water-Based Electrospinning Process and Their Application in Photocatalysis. *Nanomaterials* **2020**, *10*, 882. [\[CrossRef\]](#) [\[PubMed\]](#)
33. Li, Y.; Zou, X.; Huang, X.; Shi, J.; Zhao, J.; Holmes, M.; Hao, L. A new room temperature gas sensor based on pigment-sensitized TiO₂ thin film for amines determination. *Biosens. Bioelectron.* **2015**, *67*, 35–41.
34. Chen, D.; Li, B.; Pu, Q.; Chen, X.; Wen, G.; Li, Z. Preparation of Ag-AgVO₃/g-C₃N₄ composite photo-catalyst and degradation characteristics of antibiotics. *J. Hazard. Mater.* **2019**, *373*, 303–312. [\[CrossRef\]](#) [\[PubMed\]](#)
35. Wu, L.; Wang, Q.; Zhuang, T.; Li, Y.; Zhang, G.; Liu, G.; Fan, F.; Shi, L.; Yu, S. Single crystalline quaternary sulfide nanobelts for efficient solar-to-hydrogen conversion. *Nature Commun.* **2020**, *11*, 5194. [\[CrossRef\]](#)
36. Bai, S.; Liu, H.; Sun, J.; Tian, Y.; Chen, S.; Song, J.; Luo, R.; Li, D.; Chen, A.; Liu, C. Improvement of TiO₂ photocatalytic properties under visible light by WO₃/TiO₂ and MoO₃/TiO₂ composites. *Appl. Surf. Sci.* **2015**, *338*, 61–68. [\[CrossRef\]](#)
37. Rahmawati, F.; Putri, F.R.; Masyku, A. The Photocatalytic Activity of ZnS-TiO₂ on a Carbon Fiber Prepared by Chemical Bath Deposition. *Open Chem.* **2019**, *17*, 132–141. [\[CrossRef\]](#)
38. Zhang, Y.; Luo, L.; Shi, Z.; Shen, X.; Peng, C.; Liu, J.; Chen, Z.; Chen, Q.; Zhang, L. Synthesis of MoS₂/CdS Heterostructures on Carbon-Fiber Cloth as Filter-Membrane—Shaped Photocatalyst for Purifying the Flowing Wastewater under Visible-Light Illumination. *Chem. Cat Chem.* **2019**, *11*, 2855–2863.
39. Liu, J.; Liu, Y.; Li, N.; Han, Y.; Zhang, X.; Huang, H.; Lifshitz, Y.; Lee, S.; Zhong, J.; Kang, Z. Metal-free efficient photocatalyst for stable visible water splitting via a two-electron pathway. *Science* **2015**, *347*, 970–974. [\[CrossRef\]](#)
40. Yagi, M.; Maruyama, S.; Sone, K.; Nagai, K.; Norimatsu, T. Preparation and photoelectrocatalytic activity of a nano-structured WO₃ platelet film. *J. Solid State Chem.* **2008**, *181*, 175–182. [\[CrossRef\]](#)
41. Pearson, R. Absolute electronegativity and absolute hardness of Lewis acids and bases. *J. Am. Chem. Soc.* **1985**, *107*, 6801–6806. [\[CrossRef\]](#)
42. Zhang, W.; Jiang, L.; Ye, J. Photoelectrochemical Study on Charge Transfer Properties of ZnO Nanowires Promoted by Carbon Nanotubes. *J. Phys. Chem. C* **2009**, *113*, 16247–16253. [\[CrossRef\]](#)
43. Zhang, W.; Jiang, L.; Yu, Y.; Wei, X. Electrodeposition of Polyaniline onto TiO₂ Nanoparticles/Multiwalled Carbon Nanotubes for Visible Light Photoelectrocatalysis. *J. Nanosci. Nanotechnol.* **2014**, *14*, 7032–7037. [\[CrossRef\]](#) [\[PubMed\]](#)